DTU Library

Numerical Considerations to Improve the Reduced-Order Model Approach for Antenna Measurements

Corre, S.; Coq, L. Le; Mezieres, N.; Mattes, M.; Fuchs, B.

Link back to DTU Orbit

Numerical Considerations to Improve the Reduced-Order Model Approach for Antenna Measurements

S. Corre, L. Le Coq, N. Mézières
IETR - UMR CNRS 6164
Université de Rennes 1
Rennes, France
samuel.corre@univ-rennes1.fr

M. Mattes
Electromagnetic Systems Section
Technical University of Denmark
Lyngby, Denmark

B. Fuchs
Federal Office of Communications
Biel, Switzerland

Abstract—The determination and validation of the radiation properties of antennas are necessary tasks in their development It often calls for the sophisticated and costly evaluation of the 3D radiation pattern. The Reduced-Order Model (ROM) has been successfully applied in antenna measurements to reduce the required number of sampling points over the scan surface, leading to faster field acquisitions. It is constructed by the Singular Value Decomposition (SVD) of the radiation matrix computed from the equivalent, or Huygens, surface principle, using the method of moments. In this article, we propose several studies aiming for a better and easier use of this technique as it deeply relies on numerical computations. In particular, the evaluated number of degrees of freedoms is investigated relatively to the dimensions of the equivalent surface, the area of the observation region and the stability with respect to various parameters. Also, the use of the Randomized Singular Value Decomposition (RSVD) to speed up the computation time of the ROM is studied. Validations based on both simulation and experimental data are shown.

I. Introduction

The characterization of antennas is an important but time consuming task to validate the design of complex radiating structures. The duration of the process can be mitigated by reducing the number of field samples. The ROM approach has already been applied successfully to this end [1] [2]. It constructs a reduced field expansion basis tailored to both the geometry of the Antenna Under Test (AUT) and the measurement surface.

The common approaches to expand the sampled radiated field uses analytical basis, like Spherical Waves (SW) [3], planar waves [4] or Green's functions [5]. The size of that basis is determined by a maximum variation hypothesis, as in the well known Nyquist sampling theorem. The properties of these functions have been exploited to reduce the number of sampling points in various manners, as for example by using sparse SW reconstruction [6], [7], enabling a sample reduction of factor 2 as compared to the so-called Nyquist sampling rate.

More recently, methods based on a numerically constructed basis have arisen. In [8], the authors use simulations of the same reflector antenna with slightly different configurations to provide a tailored field expansion basis. The ROM is computed by the truncation of the SVD of the radiation matrix from an equivalent surface enclosing the sources, as shown and validated on reduced field samples in planar [1] or with spherical [9] configurations in the near and far field. It provides a compressed basis by harnessing the geometry of the AUT and the distribution of the sampling points.

In this paper, the ROM approach for antenna measurements is further developed to extend its range of application and to improve its efficiency. The numerical basis is investigated with a particular focus on its size, which determines the number of sampling points, and the expected characterization accuracy. Last but not least, the computation of the ROM requires to perform a SVD whose computational cost may be intractable for electrically large antennas. Therefore, an algorithm allowing for faster, but approximate decomposition, called the Randomized SVD (RSVD) [10], is employed and accuracy losses are discussed.

The article is organized as follows. The construction of the ROM is described in Section II. The studies on the truncation order of the basis are led in Section III. The use of the RSVD for faster ROM computations is investigated in Section IV. Conclusions and perspectives are given in Section V.

II. Construction of the Reduced-Order Model

A. Surface Equivalence Principle

The electromagnetic field $(\mathbf{E}, \mathbf{H})$ radiated by sources $(\mathbf{J}, \mathbf{M})$ delimited by a closed surface Σ can be rewritten in terms of equivalent surface electric and magnetic currents $(\mathbf{J}_{eq}, \mathbf{M}_{eq})$, as explained in [11]. This is known as the equivalent surface, or Huygens', principle. Different formulations exist depending on the constraints imposed on the interior part of Σ. In this paper, they are left unconstrained to ease the radiation pattern characterization, as observed in [12]. Here, the surface Σ is a 2D rectangle, therefore the observation region is concentrated on one side, as in [1] and sketched in Fig. 1.
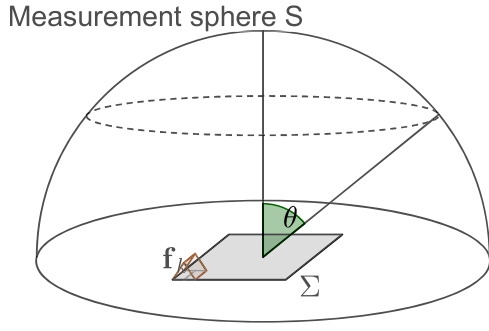
Fig. 1. Representation of the equivalent planar surface Σ, the observation area S, a basis function $\mathbf{f}$, and the observation angle θ.

B. Matrix Formulation

The aforementioned principle is used to translate the problem of characterizing the radiated field into a linear system of equations of reduced size as compared to conventional approaches. A more detailed description is available in [9].

1) Boundary Element Method: The electric field radiated by the equivalent surface currents $(\mathbf{J}_{eq}, \mathbf{M}_{eq})$ over Σ into a source-free homogeneous region, characterized by its permeability μ and permittivity ε and employing the Lorenz gauge, is given by the following integral operator

$$
\begin{aligned}
\mathbf{E}(\mathbf{r}) = {} & j\omega\mu \int_{\Sigma} g(\mathbf{r}, \mathbf{r}') \mathbf{J}_{eq}(\mathbf{r}') d\sigma' \\
& - \frac{1}{j\omega\varepsilon} \int_{\Sigma} \mathbf{grad_r} g(\mathbf{r}, \mathbf{r}') \mathrm{div}\, \mathbf{J}_{eq}(\mathbf{r}') d\sigma' \\
& - \int_{\Sigma} \mathbf{rot_r} \big(g(\mathbf{r}, \mathbf{r}') \mathbf{M}_{eq}(\mathbf{r}') \big) d\sigma'
\end{aligned}
\tag{1}
$$

where ω is the angular frequency and g the scalar free-space Green function, $g(\mathbf{r}, \mathbf{r}') = \frac{e^{-jk|\mathbf{r}-\mathbf{r}'|}}{4\pi|\mathbf{r}-\mathbf{r}'|}$. The vector $\mathbf{r}$ is the observation point, $\mathbf{r}'$ is the integration variable over Σ and a positive time convention is used ($e^{j\omega t}$). The notations $\mathbf{grad_r}$ and $\mathbf{rot_r}$ mean that the derivatives are taken with respect to the observation position $\mathbf{r}$ only. The equation (1) is valid for all observation points $\mathbf{r}$ outside the volume V enclosed by Σ.

The equivalent current distributions $(\mathbf{J}_{eq}, \mathbf{M}_{eq})$ are expanded into a set of known basis functions $\mathbf{f}_k, k = 1, \ldots, K$ defined on a mesh over Σ

$$
\mathbf{J}_{eq}(\mathbf{r}') = \sum_{k=1}^{K} \mathrm{j}_k \mathbf{f}_k(\mathbf{r}'), \ \mathbf{M}_{eq}(\mathbf{r}') = \eta \sum_{k=1}^{K} \mathrm{m}_k \mathbf{f}_k(\mathbf{r}').
\tag{2}
$$

where the complex coefficients j_k and m_k determine the equivalent currents and consequently the radiated field. The multiplication by the wave impedance η improves the conditioning of the problem by equalizing the order of magnitude of both currents, as advocated in [13].

2) Discretization of the Radiation Operator: The simultaneous use of the basis functions $\mathbf{f}_k$ and of a quadrature rule allows for the computation of a matrix $\mathbf{A}$ representing the radiation operator given in (1). In this paper, the meshes are made of square cells and the considered basis functions $\mathbf{f}_k$

in (2) are the so-called *rooftops*, represented in Fig. 1. The Gauss-Legendre quadrature with 4 points is used as numerical integration method.

3) Linear System for Characterization: Finally, the discretization of the radiation operator in (1) leads to the following linear system

$$
\begin{bmatrix} \mathbf{E}_{\theta} \\ \mathbf{E}_{\varphi} \end{bmatrix} = \begin{bmatrix} \mathbf{A}_{J,\theta} & \eta\mathbf{A}_{M,\theta} \\ \mathbf{A}_{J,\varphi} & \eta\mathbf{A}_{M,\varphi} \end{bmatrix} \begin{bmatrix} \mathbf{j} \\ \mathbf{m} \end{bmatrix}
\tag{3}
$$

where $\mathbf{E}_{\theta}$ contains the θ-component of $\mathbf{E}$ at the observation positions, $\mathbf{A}_{J,\theta}$ the θ-component of the electric current distribution in the equation (1) for each basis functions $\mathbf{f}_k$. The other quantities are defined similarly. The radial component, $\mathbf{E}_r$, is not considered since it is not measured. The vectors $\mathbf{j}$ and $\mathbf{m}$ gather all the coefficients of the equivalent current expansions, j_k and m_k. The system (3) is denoted by $\mathbf{y} = \mathbf{A}\mathbf{x}$ thereafter.

C. Compressed Basis by Reduced-Order Model

The radiation matrix $\mathbf{A}$ is poorly conditioned since a given field in $\mathbf{y}$ can be described by an infinity of equivalents currents. However, it can be approximated by a lower rank matrix $\mathbf{A}_T$, deduced from the T largest singular values and vectors computed by the SVD of $\mathbf{A}$

$$
\mathbf{A}_T = \mathbf{U}\mathbf{S}_T\mathbf{V}^H
\tag{4}
$$

where $\mathbf{V}^H$ is the conjugate transpose of $\mathbf{V}$. In particular, $\mathbf{U}$ and $\mathbf{V}$ are unitary matrices; their columns form an orthonormal basis of the radiated fields by the surface Σ into the sampling and the associated equivalent current distributions over the equivalent surface Σ, respectively, as displayed in Fig. 2. The matrix $\mathbf{S}$ is diagonal and contains the singular values, the coupling between the modes in $\mathbf{U}$ and their corresponding currents in $\mathbf{V}$. The matrix $\mathbf{S}_T$ is simply $\mathbf{S}$ where the diagonal elements after the T-th entry are set to zero.
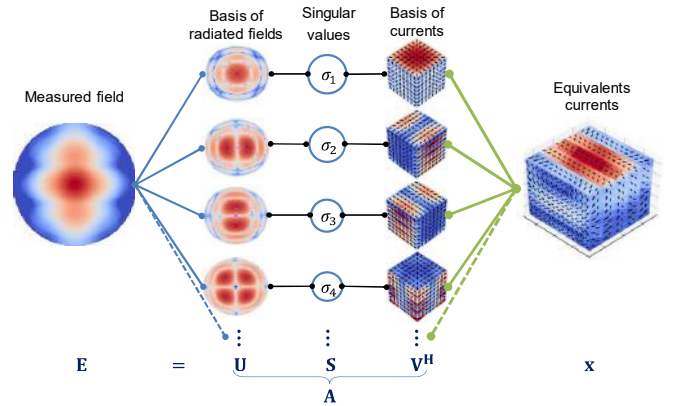

Fig. 2. Physical interpretation of the SVD of the radiation operator from a box-type equivalent surface into an hemisphere.

Since we are only interested in the radiated field, the expansion into the modes contained in the T first columns of $\mathbf{U}$, written as $\mathbf{U}_T$, is performed, leading to

$$
\mathbf{y} = \mathbf{U}_T \boldsymbol{\nu}
\tag{5}
$$

where $\boldsymbol{\nu}$ is the new unknown vector of length T. The residual of (5) is determined by the truncation order T, the number of modes. The order T is determined from the normalized singular values as

$$\max_{T>0} \frac{\sigma_{T-1}}{\sigma_0} \geq 10^{s/20}, \qquad (6)$$

where s is the desired dynamic range, or accuracy level, in dB, as in [9].

III. TRUNCATION ORDER OF THE BASIS

The order of the model is the truncation order T. It corresponds to the number of degrees of freedom of the field, as defined by Bucci in [14], given by

$$T_B = 2\chi \frac{\mathcal{A}(\Sigma)}{(\lambda/2)^2} \qquad (7)$$

where $\mathcal{A}(\Sigma)$ is the area of the equivalent surface and χ an oversampling factor. An *a priori* evaluation of T enables a simple and convenient estimation of the required number of samples M_s. It has been shown in [2] that for a closed equivalent surface, such as a box, a sphere, or a cylinder, and a full sphere measurement,

$$M_s = \chi_s T \qquad (8)$$

where χ_s is an oversampling factor. In this study, the equivalent surface is a plane and the observation area S is a part of the sphere in the far field, as in Fig. 1.

A. Estimations from Geometrical and Physical Parameters

The radiation matrix **A** and its singular values depend strongly on the geometry of both the observation region S and the equivalent surface Σ. The first one is defined by a cone through a solid angle bounded by $\max(\theta)$ and the sampling strategy. The equivalent surface Σ is a plane of dimensions (x, y) and placed at $z = 0$. This surface is meshed by square cells with edge length $\Delta < \frac{\lambda}{2}$.

1) Role of the maximum observation angle: The distribution of the singular values is displayed for a plane of size $(x, y) = (12, 12)\lambda$ and various $\max(\theta)$ as in Fig. 3. The singular values decrease almost linearly after a given index k when $\max(\theta) < 90°$. Since the equivalent surface is planar and the field is measured in half a sphere, constraining one half of the space boils down to determine the field everywhere. When $\max(\theta) > 90°$ a symmetry is imposed which improves the conditioning of the problem and induces a slower decay of the singular value distribution. However, no degrees of freedom are added, so the criterion (7) is no longer directly related to the accuracy of the resolution of system (5), determined by the dynamic range s.

2) Role of the expected dynamic range s: The truncation index T given by (6) for several square equivalent surfaces of dimensions (x, y) are shown relatively to the expected accuracy level s in Fig. 4. It can be observed that the truncation index T grows linearly according to $\mathcal{A}(\Sigma)$ and decreases almost linearly with respect to s, corresponding to the linear decrease of the singular values in Fig. 3.
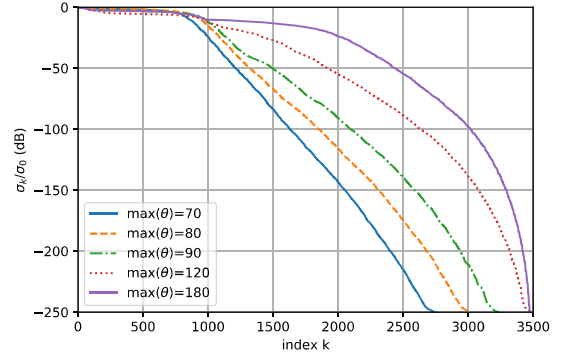

Fig. 3. Normalized singular value distributions of the radiation matrix from a square planar surface of side 12λ relatively to the observation region given by $\max(\theta)$.
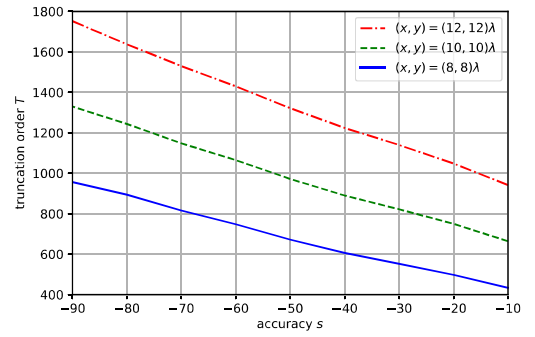

Fig. 4. Truncation order T for several equivalent surfaces Σ and criterion s, with $\lambda = 0.01$, $\Delta = 0.004$ and $\max(\theta) = 80°$

3) Comparison with the analytical criterion: Finally, the computed truncation index T given by the equation (6) and the estimation T_B given by the equation (7) are compared in Fig. 5. Our numerical approach retrieves the results predicted in the analytical work of Bucci *et al.* [14]. It must be added that the numerical criterion (6) is mostly valid for sufficiently large antenna. Therefore larger oversampling factors χ are required when the domain is small. Also, the aspect ratio of the planar domain Σ has an important role in the estimation of T as shown in Table I, with $s = -50$ dB. A possible explanation can be formulated as follows: the theory of antenna arrays claims that, for a given area, the complexity of the radiation pattern in a fixed cutting plane plane depends on the unit elements distribution. On the other hand, the igloo sampling provides an almost uniform distribution on the observation region. It implies that some part of the sphere might be oversampled/undersampled, and therefore induces different singular value behaviors. This point is under investigation and will be discussed in future works.

B. Validations with Simulation Data

1) Reconstruction accuracy: To evaluate the quality of the reconstructions, the comparison between the radiation pattern
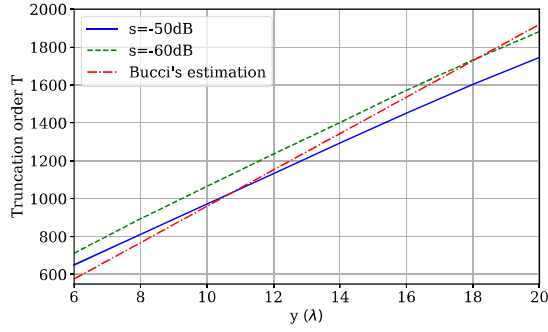
Fig. 5. Comparison of the truncation order T given by the numerical (6), in green and blue, and the analytical (7), in red, criteria for $x = 10\lambda$ and a maximal angle $\max(\theta) = 80°$ as a function of the size y.

Fig. 6. Metasurface type antenna [15] of dimension 12λ at 30 GHz.

TABLE I
TRUNCATION ORDERS T FOR $\mathcal{A}(\Sigma) = 64\lambda^2$.

$(x, y)/\lambda$	$(1, 64)$	$(2, 32)$	$(4, 16)$	$(8, 8)$
T	1214	936	796	726

of reference $\mathbf{y}$ and the reconstructed one $\widetilde{\mathbf{y}}$ is achieved point-wise by the complex error signal defined as

$$\text{Error}(\mathbf{y}, \widetilde{\mathbf{y}}) = \frac{|\mathbf{y} - \widetilde{\mathbf{y}}|}{\|\mathbf{y}\|_\infty}. \quad (9)$$

The equivalent noise level (ENL) is defined as the mean of that signal error. Both errors are given in dB.

2) Methodology: The radiation matrix $\mathbf{A}$ is computed on a dense igloo sampling for $\max(\theta) = 80°$. Two reduced basis sizes are deduced from the analytical criterion T_B in (7) and the numerical one based on singular value inspection (6). A subsampling whose size is determined by (8) is used to emulate a reduced measurement set. For both basis, the corresponding linear system (5) is solved. Finally, the field is reconstructed on the initial dense sampling and comparisons with simulation data are performed. An oversampling factor $\chi_s = 1.2$ is chosen.

3) Applications: The approach and the observations are validated through simulations of two antennas in the far field. The first antenna is an E-plane horn simulated at 3 GHz, with $\Sigma = (1.5, 2.25)\lambda$, and the second antenna is a metasurface antenna [15] simulated at 30 GHz (Fig. 6), with $\Sigma = (12, 12)\lambda$. The observation region is given by $\max(\theta) = 80°$. Reconstructions for the metasurface antenna are shown in Fig. 7 and ENL values in Table II.

The results in Table II confirm that the analytical estimation T_B in (7) is inappropriate for the horn antenna because of its small size whereas it provides a sufficient *a priori* estimation for the metasurface antenna, which is electrically larger. The truncation order (6) allowed for accurate reconstructions in all cases. For the sake of completeness, two discretization steps (square cell width) are considered. For a small spatial step of discretization $\Delta = \lambda/4$, the approximation has a
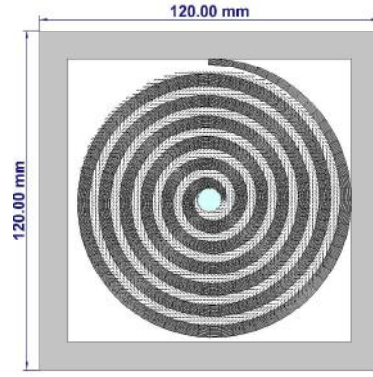
TABLE II
COMPARISON OF THE ANALYTICAL AND NUMERICAL TRUNCATION
ORDERS T.

Horn antenna		
	T_B (7)	T (6)
T ($\Delta = \lambda/4$)	70	100
T ($\Delta = \lambda/8$)	70	112
ENL ($\Delta = \lambda/4$) [dB]	-22.49	-65.05
ENL ($\Delta = \lambda/8$) [dB]	-24.17	-67.52
Metasurface antenna		
	T_B (7)	T (6)
T ($\Delta = \lambda/4$)	1382	1296
T ($\Delta = \lambda/8$)	1382	1312
ENL ($\Delta = \lambda/4$) [dB]	-69.43	-56.29
ENL ($\Delta = \lambda/8$) [dB]	-70.08	-57.37

good accuracy, which is not improved if a smaller step (e.g. $\Delta = \lambda/8$) is chosen.

IV. FAST MODEL COMPUTATION

The ROM approach requires the computation of the SVD of the radiation operator. Computing the complete SVD is not only computationally demanding but also not necessary, since only the T dominant modes are kept with the ROM approach. For that purpose, a partial SVD can be approximated using the RSVD based on the *a priori* truncation index T_B in eq. (7).

For m sampling points and n square cells, the radiation matrix $\mathbf{A}$ has $2m$ lines (2 polarizations per sampling point) and $2(2n)$ columns (2 directions per cell for both types of currents). Consequently, the SVD of $\mathbf{A}$ has a complexity of $\mathcal{O}(m^2 n)$, which is larger than $4xy/\lambda$ for $\Delta \leq \lambda/2$. For the metasurface antenna, the matrix has a size of 8660×9024 for $\Delta = \lambda/4$ representing $\mathcal{O}(6 \times 10^{11})$ operations.

A. Randomized Singular Value Decomposition

To compute the SVD of large matrices, an efficient algorithm is the RSVD computation method proposed in [10] with a complexity of $\mathcal{O}(T\tau_{mult} + T^2(m+n))$, with τ_{mult} the cost of a matrix-vector multiplication, and T the truncation order

(6). With *a priori* estimations $m = M_s$, and $n = T$, we have a complexity of $\mathcal{O}(T\tau_{mult} + T^3(\chi_s + 1))$. After that partial SVD, another truncation is performed at index T given by the criterion (6).

B. Numerical Performances

The execution time (in seconds) of RSVD and SVD methods and their corresponding field reconstruction performances are compared. On the one hand, the whole SVD of $\mathbf{A}$ is computed, and $\mathbf{U}_T$ is derived with T given by the numerical criterion (6). On the other hand, we use the *a priori* estimation of T_B given analytically by eq. (7) to perform the RSVD algorithm, and the resulting matrices are truncated according to criterion (6), if $T < T_B$. Simulations have been performed on an Intel Xeon CPU E5-2620 v4 2.10GHz × 32 processor, the SVD algorithm comes from the scipy linalg library, and the RSVD algorithm from the sklearn library, with Python. In that simulation, the radiated matrix $\mathbf{A}$ is computed over a dense igloo sampling of size 8660 containing the measurement sampling of size $M_s = 2194$. We study three different mesh refinements Δ. The results are summarized in Table III.

For a coarse discretization, Δ roughly smaller than $\lambda/2$, the RSVD reduces the execution time but introduces significant errors in the ENL. The interest of the RSVD arises for finer discretizations. Indeed, when $\Delta = \lambda/4$, the ENL is the same for both methods but the computational time is already 4 times smaller for the RSVD approach. The corresponding reconstructions are shown in the cutting plane in Fig. 7. For a very small discretization step $\Delta = 0.00125 = \lambda/8$, the execution time reduces drastically from 796 to 136s. There is no significant gain in accuracy. It clearly illustrates the savings in computational efforts provided by the RSVD.

TABLE III
COMPARISON OF RSVD TIME FOR THE METASURFACE TYPE ANTENNA (IN SECONDS).

	RSVD	SVD
$\Delta = 0.004 \approx \lambda/2$		
Execution time (s)	20	31
ENL (dB)	-37.53	-47.15
$\Delta = 0.0025 = \lambda/4$		
Execution time (s)	59	257
ENL (dB)	-48.42	-48.42
$\Delta = 0.00125 = \lambda/8$		
Execution time (s)	136	796
ENL (dB)	-50.41	-50.42

C. Experimental validation

The considered antenna is a pillbox antenna issued from a collaboration between IETR and KTH [16] and measured in the M²ARS facilities of IETR, represented in Fig. 8. It consists of a electrically large square with slots operating around 230 GHz whose beam can be scanned in the elevation plane. An equivalent surface $\Sigma = (20, 20)\lambda$ with a discretization step Δ between $\lambda/2$ and $\lambda/3$ is considered. The standard SVD
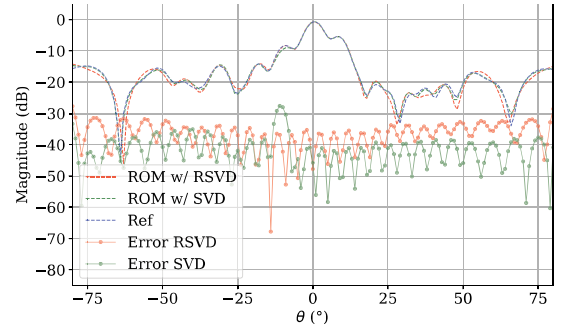
(a) Polarization $\mathbf{E}_\theta$
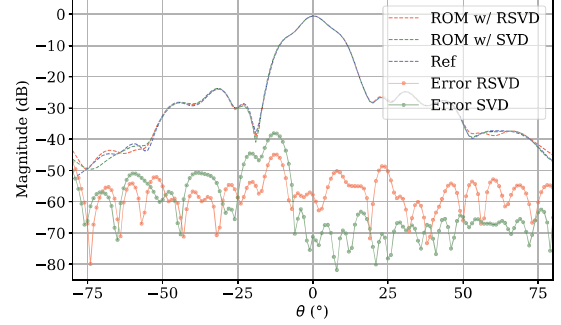
(b) Polarization $\mathbf{E}_\varphi$

Fig. 7. Metasurface antenna at 30 GHz: reconstruction of the field for $\varphi = 0°$

is performed in 225s and the RSVD in 138s, for an ENL of -49.78 dB for both methods. Finally, reconstructions of the main cutting planes for both polarizations are shown in Figs. 9 and 10. Approximation given by classical SVD is better because of the electrical size of the antenna and its pointing direction according to the planar domain Σ. That case will be investigate further to improve the method.
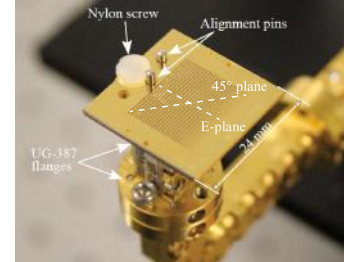

Fig. 8. Pillbox type antenna, by IETR and KTH [16] operating at 230 GHz.

V. CONCLUSION

The use of the Reduced-Order Model approach has been investigated to speed up antenna measurements and improved with respect to previously existing works. The number of modes required for the radiated field expansion has been related with the planar surface dimensions and the observation region. It has also been compared to an existing analytical criterion. A method for a partial Singular Value Decomposition has been used successfully and has been shown to greatly
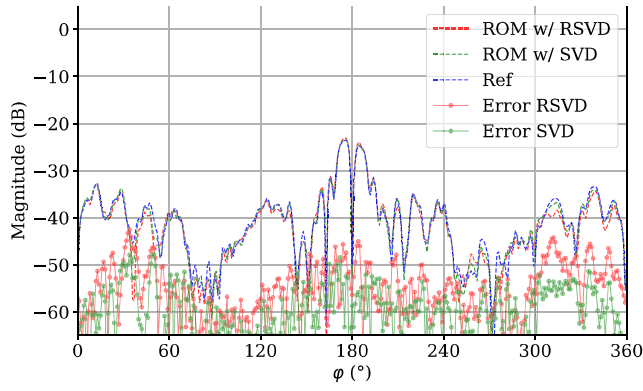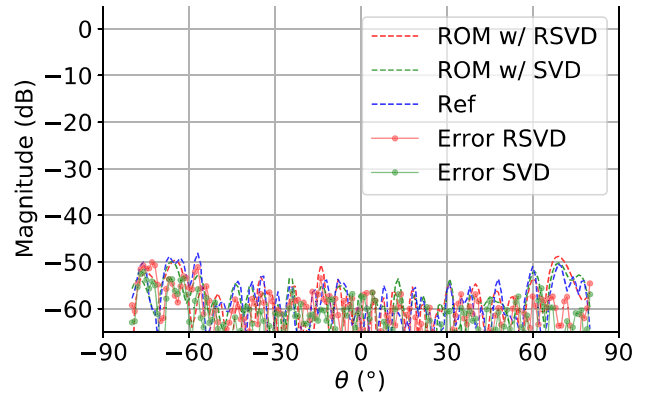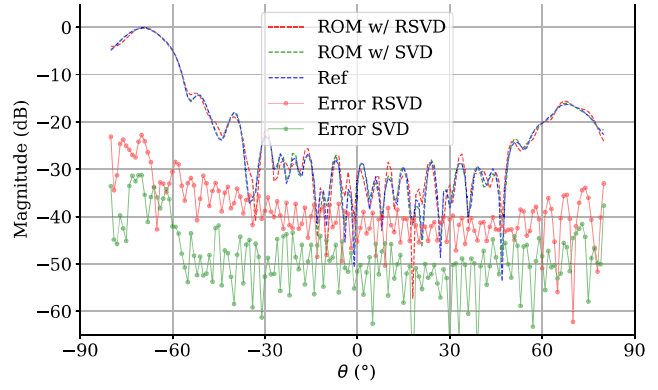
(a) Polarization $\mathbf{E}_\theta$
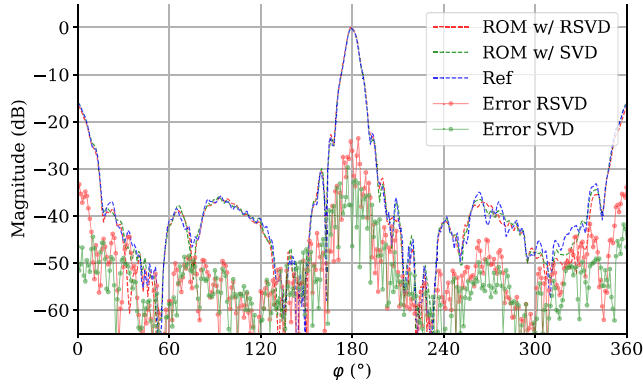
(b) Polarization $\mathbf{E}_\varphi$

Fig. 9. Pillbox type antenna at 230 GHz: reconstruction of the field for $\theta = 68°$

(a) Polarization $\mathbf{E}_\theta$

(b) Polarization $\mathbf{E}_\varphi$

Fig. 10. Pillbox type antenna at 230 GHz: reconstruction of the field for $\varphi = 0°$

reduce the computationnal cost of the procedure, enabling the characterization of electrically larger radiating structures..

REFERENCES

[1] B. Fuchs and A. Polimeridis, "Reduced-order models for fast antenna characterization," *IEEE Trans. on Antennas and Propag.*, vol. 67, no. 8, pp. 5673–5677, Aug. 2019.

[2] N. Mézières, M. Mattes, and B. Fuchs, "Antenna characterization from a small number of far-field measurements via reduced-order models," *IEEE Trans. on Antennas and Prop.*, vol. 70, pp. 2422 – 2430, 2022.

[3] J. Hald, J. Hansen, F. Jensen, and F. Larsen, *Spherical Near Field Antenna Measurements*. Peter Peregrinus, 1988.

[4] S. Gregson, J. McCormick, and C. Parini, *Principles of Planar Near-Field Antenna Measurements*. IET, 2007, vol. Series 53.

[5] O. M. Bucci and G. Franceschetti, "On the spatial bandwidth of scattered fields," *IEEE Trans. on Antennas and Propag.*, vol. 35, no. 12, pp. 1445–1455, 1987.

[6] R. Cornelius, D. Heberling, N. Koep, A. Behboodi, and R. Mathar, "Compressed sensing applied to spherical near-field to far-field transformation." Davos: Eur. Conf. Antennas Propag., 2016, pp. 1–4.

[7] B. Fuchs, L. Le Coq, S. Rondineau, and M. Migliore, "Fast antenna far field characterization via sparse spherical harmonic expansion," *IEEE Trans. on Antennas and Propag.*, vol. 65, no. 10, pp. 5503–5510, Oct. 2017.

[8] G. Giordanengo, M. Righero, F. Vipiana, M. Sabbadini, and G. Vecchi, "Fast antenna testing with reduced near field sampling," *IEEE Trans. on Antennas and Propag.*, vol. 62, no. 5, pp. 2501–2513, May 2014.

[9] N. Mézières, M. Mattes, and B. Fuchs, "Characterization of antenna far-field pattern from a minimum number of samples," *AMTA*, 2021.

[10] T. J. A. Halko N., Martinsson P. G., "Finding structure with randomness: Probabilistic algorithms for constructing approximate matrix decompositions," vol. 53, no. 2, pp. 217–288, 2011.

[11] R. F. Harrington, *Time-Harmonic Electromagnetic Fields*. IEEE-Press, 2001. [Online]. Available: http://dx.doi.org/10.1109/9780470546710

[12] J. L. Araque Quijano and G. Vecchi, "Field and source equivalence in source reconstruction on 3d surfaces," *Progress In Electromagnetics Research*, vol. 103, pp. 67 – 100, 2010.

[13] ——, "Improved-accuracy source reconstruction on arbitrary 3-d surfaces," *IEEE Antennas and Wireless Propagation Letters*, vol. 8, pp. 1046–1049, 2009.

[14] O. M. Bucci, C. Gennarelli, and C. Savarese, "Representation of electromagnetic fields over arbitrary surfaces by a finite and nonredundant number of samples," *IEEE Trans. on Antennas and Propag.*, vol. 46, no. 3, pp. 351–359, March 1998.

[15] D. Gonzalez-Ovejero, N. Chahat, R. Sauleau, G. Chattopadhyay, S. Maci, and M. Ettorre, "Additive Manufactured Metal-Only Modulated Metasurface Antennas," *IEEE Trans. Propag.*, vol. 66, no. 11, pp. 6106–6114, 2018.

[16] A. Gomez-Torrent, M. Garcia-Vigueras, L. Le Coq, A. Mahmoud, M. Ettorre, R. Sauleau, and J. Oberhammer, "A low-profile and high-gain frequency beam steering subterahertz antenna enabled by silicon micromachining," *IEEE Trans. on Antennas and Propag.*, vol. 68, no. 2, pp. 672–682, Aug. 2020.